



Structural responses of energy storage pile foundations under thermal-mechanical loadings

Madina Bimaganbetova^a, Dichuan Zhang^{a,*}, Jong Kim^a, Chang-Seon Shon^a, Deuckhang Lee^b

^a Department of Civil and Environmental Engineering, School of Engineering and Digital Sciences, Nazarbayev University, Nur-Sultan, Kazakhstan

^b Department of Architectural Engineering, Chungbuk National University, Cheongju, South Korea

ARTICLE INFO

Keywords:

Structural response
Thermal-mechanical loading
Energy storage pile foundation
Compressed air energy storage

ABSTRACT

Recently studies have investigated feasibilities to configure pile foundations as energy storage media using a small-scale compressed air energy storage technology. These studies consider that storage temperatures of compressed air can be lowered entirely down to ambient temperatures through a cooling process. This assumption may not be feasible and economical due to the efficiency of the cooling process. As an alternative option, a higher storage temperature can be allowed by reducing the cooling time, which can cause additional thermal-mechanical loadings to the pile foundation. This paper investigates structural responses of reinforced concrete pile foundations subjected to combined structural, compressed air pressure, and thermal-mechanical loadings through nonlinear dynamic heat transfer and thermal-mechanical analyses. Several parameters were studied, including pile spacing, pile inner diameters, and concrete grades. Analysis results show that thermal-mechanical loading can reduce critical tensile stresses and change stress distributions in the pile section originated from compressed air pressure. Design recommendations were made to determine an optimal storage temperature and an allowable loading cycle for the energy storage pile foundation.

1. Introduction

Recently research has been applied on investigating new technologies to configure pile foundations with dual functionality for improving energy efficiencies of building structures. One of the technologies is to treat the pile foundation as a heat-exchanger, the so-called energy pile, to enable an exchange of heat with the surrounding soil by circulating water inside the pile [1]. The energy pile can be used to heat up or cool down buildings in addition to transferring structural loads to the soil. Extensive research has been conducted on the energy pile regarding the thermal-mechanical effect on the pile and surrounding soil [2–5]. Another technology uses the pile foundation as a medium, termed here as energy storage pile foundation, to store renewable energy generated from solar panels attached to buildings [6]. Renewable energy usually has an intermittent nature which may not match energy demands [7]. Therefore, the energy storage pile foundation is intended to utilize a small-scale compressed air energy storage (CAES) technology to store renewable energy in the form of compressed air when the renewable energy supply is more than the demand. The compressed air stored in a pile can be timely released to generate electric power when renewable energy is unavailable.

The existing compressed air energy storage technology has been commercialized for several power plants, including Hunt, Germany; McIntosh, Alabama, US; Ganiex, Texas, US; Goder, Ontario, Canada. These power plants are using large-scale underground caverns as storage media. The storage volume is relatively large, and the storage pressure is not significant [8]. For the proposed energy storage pile foundation, a small-scale CAES is required due to the limited storage volume, resulting in a large storage pressure. The feasibility of the energy storage pile foundation has been investigated for different construction materials including reinforced concrete piles [9,10], steel piles [11,12], and steel-concrete composite piles [13]. Previous studies consider that the compressed air can be cooled entirely down to an ambient temperature through a cooling process before entering the pile for storage. The pile foundation can be therefore subjected to combined structural and storage pressure loadings. This pressure loading can generate significant tensile stresses inside the pile, which causes challenges in ensuring the structural safety of the pile, particularly for the reinforced concrete pile foundation [9]. Even though high strength fiber-reinforced concrete can provide enough strength to resist these tensile stresses, the pile section is under an unfavorable pure tension state [10].

The cooling process in the CAES technology has its own operation

* Corresponding author.

E-mail address: dichuan.zhang@nu.edu.kz (D. Zhang).

<https://doi.org/10.1016/j.job.2021.103539>

Received 6 August 2021; Received in revised form 11 October 2021; Accepted 27 October 2021

Available online 30 October 2021

2352-7102/© 2021 Elsevier Ltd. All rights reserved.

efficiency, which may be time-consuming and uneconomical to lower the compressed air temperature down to the ambient temperature [14]. As an alternative option, a higher storage temperature than the ambient condition can be allowed by reducing the cooling time. This higher storage temperature can cause thermal-mechanical loadings to the pile foundation in addition to the structural and storage pressure loadings considered in the previous studies. On the other hand, the thermal-mechanical loading may generate different stress conditions than those originated from the structural and the storage pressure loadings, which can be favorable to the safety of the pile foundation.

Therefore, this paper investigates structural responses of reinforced concrete pile foundations subjected to combined structural, storage pressure, and thermal-mechanical loadings. Nonlinear dynamic heat transfer analyses were first conducted to determine temperature profiles inside the pile section during energy storing-releasing cycles. Static thermal-mechanical analyses were then performed by applying the obtained temperature profile to a pile foundation model, together with the structural and storage pressure loadings. The structural response of the pile foundation was studied from the thermal-mechanical analysis, where several parameters were studied, including pile spacing, pile inner diameters, and concrete grades. Design recommendations were made to determine an optimal storage temperature and an allowable loading cycle based on the structural safety of the energy storage pile foundation obtained from the analyses.

2. Background

2.1. Thermodynamic processes of CAES

Major thermodynamic processes available for the CAES are diabatic, adiabatic, and isothermal processes depending on how the heat is managed [15]. All of them require a cooling process after or during the compression. The adiabatic process, which is more efficient than the diabatic process, is potentially suitable for the energy storage pile foundation [11]. As illustrated in Fig. 1, the adiabatic process consists of four sub-processes: (1) compression, (2) cooling, (3) heating, and (4)

expansion.

First, the ambient air (T_1, P_1) is compressed by the electric power generated from the renewable energy available for storage. Once it is compressed, the pressure and temperature of the compressed air drastically rise (T_2, P_2). This compressed air with an extra high temperature (more than 1000°C) is not practical to store inside the pile foundation. Thus, the cooling process is performed as the next step to extract the heat and store it in a heat storage medium (T_{hs}). Depending on the cooling time and efficiency, the compressed air temperature can be lowered down to the original ambient temperature as assumed in previous studies. Another option discussed in this paper is to allow the storage temperature higher than the ambient temperature by reducing the cooling time. This option enables the imposition of additional thermal-mechanical loadings to the pile foundation, which will be investigated in this paper. The cooled (entirely or partially) compressed air can then enter the pile foundation for storage (T_s, P_s). When renewable energy is not available, compressed air can be released and undergoes heating (T_3, P_3) and expansion (T_1, P_1) processes to produce electric powers for usage. More detailed discussions about thermodynamic processes of the CAES and equations for the adiabatic process can be found in Ref. [9].

2.2. Stress states in the energy storage pile

The energy storage pile foundation is configured with a hollow cross-section with an inner (d_i) and outer (d_o) diameter. Actions applied on the energy storage pile foundation are shown in Fig. 2. These actions include structural loads, constraints from surrounding soil (friction, lateral pressure, and end bearing), storage pressure loading (P_s), and storage temperature loading (T_s). The structural loads and soil constraints mainly cause vertical axial stresses (σ_v) in the pile section. This vertical axial stress is in compression as indicated in Fig. 2(b). The storage pressure loading generates compression stresses in the radial direction (σ_r) and tensile stresses in the circumferential direction (σ_θ) as shown in Fig. 2b. These tensile stresses have a nonuniform distribution. They reach a maximum value at the inner surface and gradually reduce as moving to the outer surface. The entire pile section is under tension. This

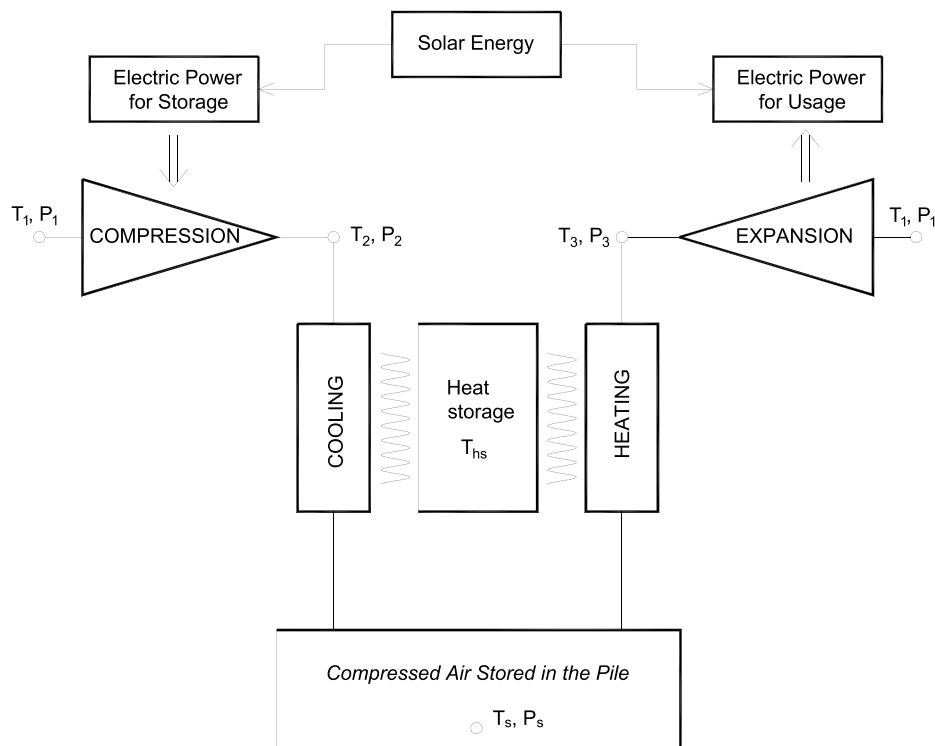


Fig. 1. Thermodynamic processes of the CAES (Modified from Ref. [9]).

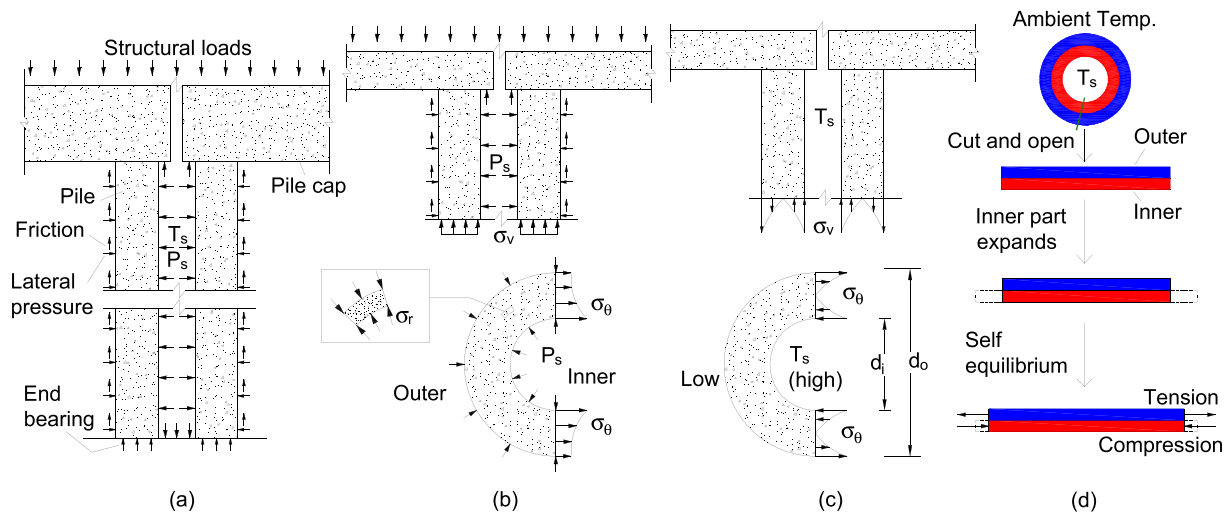


Fig. 2. Expected stress states of the energy storage pile foundation: (a) loading actions; (b) under structural loadings, soil constraints, and the storage pressure; (c) under thermal-mechanical loadings; (d) thermal-mechanical self-equilibrium.

nonuniform distribution is typically observed in thick-walled sections such as reinforced concrete piles according to Lamé’s theory [16]. For the steel energy storage pile foundation with a thin-walled section, the tensile stress is uniformly distributed [11].

The heated compressed air can increase the temperature at the inner surface of the pile section, which results in a temperature gradient as the heat require time to be transferred from the inner to the outer surfaces, and eventually to the surrounding soil. At the moment when the heated air enter the pile, the temperature at the inner part of section increases while that at the outer part remains at ambient temperature. The inner part of the pile is trying to expand due to thermal expansion while the outer part is trying to keep its original position since the temperature at the outer part has not risen yet. Because of the strain compatibility, the outer part will hold the inner part and prevent it from expanding while the inner part will then pull the outer part and make it expanding. Finally, the inner part and the outer part will reach a self-equilibrium state where the inner part is under compression (being held back by the outer part) and the outer part is under tension (being pulled out by the inner part) as seen in Fig. 2(d). Similar thermal stress distributions were observed in previous studies of hollow cylinders with heating at the inner surface from aerospace applications [17–19]. The thermal-mechanical loading on the energy storage pile foundation is quite different than that on the typical energy pile. The energy pile is usually under a uniform temperature change on the entire pile section, which causes the entire pile to elongate or shorten. This action subsequently initiates vertical compression stresses in the energy pile [3].

By utilizing the principle of superposition of the stresses from the storage pressure (Fig. 2b) and the thermal-mechanical (Fig. 2c) loadings, the tensile stress in the pile section has a potential to be reduced, and the stress distribution can be changed to a combined tension-compression distribution. Therefore, it may be beneficial to include the additional thermal-mechanical loading. However, the CAES operates in cycles with energy storing and releasing, which causes continuous changes of the temperature gradient inside the pile section. Hence, the stress states from the thermal-mechanical loading are more complicated than those illustrated in Fig. 2c (high temperature at the inner surface but low temperature at the outer surface). Finite element analyses are then required to investigate the pile section’s stress state under the aforementioned actions in combination, which will be discussed in subsequent sections.

3. Description of study

3.1. Study parameters

In the previous study on the energy storage pile foundation [9], fifteen (15) pile foundations were first designed at a medium dense sand site with a 1-m burying depth for different building geometries (number of stories and column spacing). The pile design has a fixed outer diameter ($d_o = 1\text{ m}$) but different length and spacing (s). It has been found from the previous study that the structural performance of the pile is insignificant with the pile length [9], but the heat transfer phenomena are affected by the pile spacing [20,39]. Therefore, four pile foundations with different pile spacing (s) were selected in this paper as shown in Table 1.

The previous study also indicated that the storage pressure (P_s) and temperature (T_s) increases as the inner diameter (d_i) of the pile reduces due to the decrease of the available storage volume [9]. The pile with a small inner diameter shows a better structural performance than that with a large inner diameter because the thicker section can provide more resistance and reduce the stress demand. Therefore, two pile design cases with small inner diameters were considered in this paper, including $d_i = 200\text{ mm}$ and $d_i = 300\text{ mm}$. Considering a complete parameter combination of the pile spacing (s) and the pile inner diameter (d_i), eight pile design cases were studied in this paper.

High strength fiber-reinforced concrete was considered for the energy storage pile foundation to resist the tensile stresses [10]. This paper investigates three grades of fiber-reinforced concrete with different tensile strength (f_t), compressive strength (f_c), and Young’s modulus (E_c). These properties, obtained from test results on the fiber-reinforced concrete, are listed in Table 1 [21–23].

Table 1
Study parameters.

Pile Geometries				Concrete properties			
s (m)	Pile length (m)	d_o (m)	d_i (mm)	Grade	f_c (Mpa)	f_t (MPa)	E_c (GPa)
3	6.5	1.0	200	60	61.3	4.8	39.3
4	9	1.0	300	100	99.4	6.2	42.7
5	6	1.0		150	150	8.5	45.6
6	10	1.0					

3.2. Storage pressure and temperature

Based on the energy balance for an ideal diatomic gas undergoing an isentropic adiabatic compression [24], the pressure (P_2) and temperature (T_2) after compression can be calculated by solving the following implicit equations:

$$V_s P_2^{5/7} / RC = \dot{w}_{in} \eta_1 t_{in} / 3.5R (C P_2^{2/7} - T_1) + \rho_i V_s / \mu \quad \text{Eqn. (1)}$$

$$T_2 = C P_2^{2/7} \quad \text{Eqn. (2)}$$

where, \dot{w}_{in} is the available energy for storage and V_s is the available volume for storage. The available energy for storage is dependent on the renewable energy supply and the energy consumption within a 24-h (one-day) cycle. R is the universal gas constant; C is a constant value of 10.89; t_{in} is the time for the compression; ρ_i and μ are the initial density and molar mass of the air, which are taken as 1.2 kg/m³ and 0.029 kg/mol, respectively for the air at the atmospheric pressure (0.1 MPa). η_1 is the efficiency for the compression taken as 75% [25]. The storage pressure (P_s) and temperature (T_s) can be then determined after the cooling process, as follows:

$$T_s = \gamma(T_2 - T_1) + T_1 \quad \text{Eqn. (3)}$$

$$P_s = P_2^{5/7} T_s / C \quad \text{Eqn. (4)}$$

where, γ is a cooling index to measure the relative ratio between the storage temperature (T_s) and the temperature after compression (T_2) varying between 0 and 1. This index was adopted as zero in the previous studies, where the compressed air was assumed to be cooled entirely down to the ambient temperature. However, this paper treated it as a study variable that can be varied by adjusting the cooling process. The derivations of Eqns. (1)–(4) were discussed in Ref. [9].

Using Eqns. (1)–(4), the storage pressure (P_s) and temperature (T_s) can be calculated for the pile foundations considered in this paper (Refer to Sec. 3.1). The available energy for storage were calculated from the difference between the energy supply and consumption, which were estimated for typical residential buildings in Nur-Sultan, Kazakhstan as discussed in Ref. [9]. The available volume for storage can be determined based on the pile geometries (inner diameter and length of the pile). As an example, Fig. 3 shows a 24-h (one-day cycle) storage temperature and pressure for the pile with $s = 5$ m and $d_i = 200$ mm for different γ .

As seen in Fig. 3, the storage temperature and pressure increase when the renewable energy for storage becomes available at 7:00. They continue increasing and reach the peak ($T_{s,max}$ and $P_{s,max}$) at 19:00. After the peak, renewable energy becomes unavailable. The stored energy is then gradually released to generate electric power. The storage temperature and pressure will reduce and drop back to the ambient temperature and pressure at 7:00 the next day. Multiple continuous

repeating cycles can be expected for the energy storage pile foundation. One of the goals of this paper is to determine allowable operation cycles.

3.3. Simulation models

The nonlinear dynamic heat transfer and the static thermal-mechanical analyses were performed using a general-purpose finite element software, ABAQUS. The heat transfer is unlikely affected by structural deformation in a pile, which is assumed to be in an elastic regime (i.e., small deformation). Therefore, an uncoupled sequential analysis technique was adopted. A similar approach was used to investigate thermal-mechanical behaviors of the energy pile [26]. The heat transfer analysis was first conducted to obtain the temperature distribution profile along the pile section. This temperature distribution profile was then applied together with the structural and the storage pressure (P_s , See Fig. 3b) loadings to a pile model for the thermal-mechanical analysis.

The nonlinear dynamic heat transfer analysis was performed on a two-dimensional (2D) plane strain model as shown in Fig. 4. The 2D model represents a quarter of a pile with no heat-flux passing through at the symmetric boundaries. This 2D simplification seems reasonable since the storage volume is relatively small, and the uniform distribution of the storage temperature can be assumed in the hollow space of the pile. The heat transfer at the ends of the pile is trivial and was then ignored because the inner diameter of the pile is much smaller than the pile length. For the pile section, a relatively fine mesh (20 mm × 20 mm) was applied, while for the surrounding soil, the mesh size gradually increases along the radial direction to save computational time. Interface elements with a thermal conductance of 25 W/m².°C were applied between the concrete and soil elements to model the potential micro gaps between the concrete and soil.

Dynamic analyses were performed by applying the storage temperature (T_s , see Fig. 3a) to the inner surface of the pile in multiple cycles (n). The backward Euler method with unconditional stability was used for time integration. Automatic adjustment of the time increment during the simulations was performed to limit the Courant-Fredrichs-Lewy number to be less than 1.0. The initial temperature of the pile and the surrounding soil was assumed to be 12 °C in accordance with Brandl [27].

The energy storage pile foundation adopts high strength fiber-reinforced concrete, which has an approximate thermal conductivity of 2 W/m.°C and specific heat of 940 J/kg.°C for the temperature range (20 °C–50 °C) considered in this paper based on the test results [28,29]. The thermal conductivity for medium dense sand is set as 1 W/m.°C at a mild moisture of 9% according to Abu-Hamdeh [30]. However, it reduces as the moisture content reduces due to the heating from the compressed air. Therefore, a temperature-dependent nonlinear thermal model was used. This model assumes a linear variation of thermal conductivity against the temperature: 1.0 W/m.°C at 12 °C and 0.25 W/m.°C at 100 °C, based on test results on the relationship of the moisture content and the thermal conductivity of the sand [31]. The

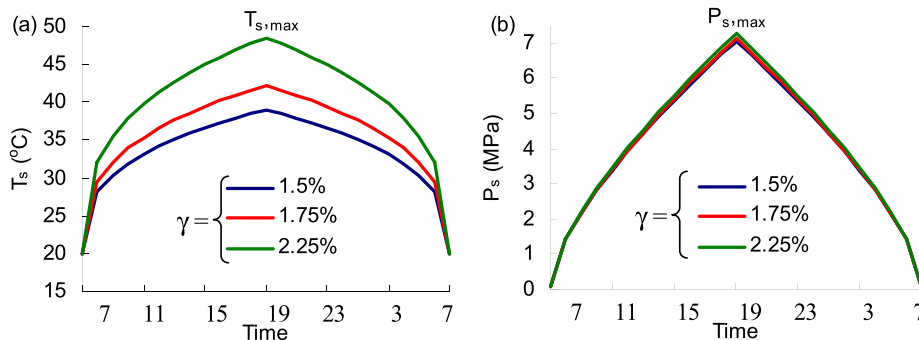


Fig. 3. 24-hour storage temperature and pressure for the pile with $s = 5$ m and $d_i = 200$ mm: (a) T_s ; (b) P_s , ($V_s = 0.2$ m³ and $w_{in} = 13.81$ KhW).

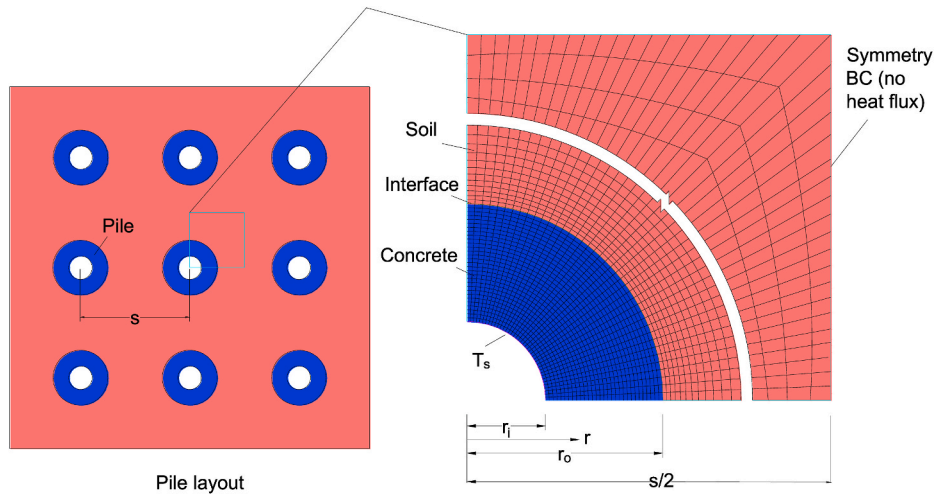


Fig. 4. 2D plane strain model for the heat transfer analysis (modified from Ref. [20]).

specific heat of the soil is selected as 1220 J/kg.°C [30]. Considering the contact condition between the concrete and soil, thermal conductance of 25 W/m².°C was assigned to the interface element [32]. The densities of concrete and soil are chosen as 2450 kg/m³ and 1600 kg/m³, respectively.

The static thermal-mechanical analysis was conducted by applying the structural, storage pressure, and thermal-mechanical loadings to a 2D axisymmetric model as shown in Fig. 5. The thermal mechanical loading was applied as the temperature profiles on the concrete section obtained from the heat transfer analysis. The 2D axisymmetric model is needed to evaluate the vertical stresses (σ_v) beside the in-plane stresses (σ_r, σ_θ). This paper aims at achieving a crack free state for the energy storage pile foundation to avoid potential air leakage. Therefore, the fiber-reinforced concrete is modeled as elastic elements with a mesh size (20 mm × 20 mm) matching the heat transfer analysis for the ease of applying the temperature profile. The elastic properties (Young's modulus shown in Table 1) were assigned to the concrete model for different concrete grades. The model has a Poisson's ratio of 0.2 and a thermal expansion coefficient of $1.5 \times 10^{-5}/^\circ\text{C}$ for typical high strength

fiber-reinforced concrete [33]. The pile cap was not modeled in the parametric study since it has little effect on the stress response in main body of the pile from preliminary analysis results.

Since the pile section is under a complicated multi-axial stress state (Refer to Fig. 2) and the concrete was modeled elastically, it is important to evaluate the stresses obtained from the analysis with a proper yield function. The yield function for a classical concrete damage plasticity model is used [34], as follows:

$$F(\sigma) - f_c = 0 \tag{Eqn. (5)}$$

where, f_c is the uniaxial compressive strength of the concrete, and $F(\sigma)$ is a scalar yield function of invariants of the stress tensor. This yield function can be expressed, as follows:

$$F(\sigma) = \frac{1}{1 - \alpha} \left(\alpha I_1 + \sqrt{3J_2} + \beta \hat{\sigma}_{max} \right) \tag{Eqn. (6)}$$

where, $\hat{\sigma}_{max}$ is algebraically maximum principal stress. I_1 and J_2 are the first invariant and the second deviatoric stress invariant, respectively. These variables can be calculated using the stress components obtained from the thermal-mechanical analysis. α and β are the dimensionless constants and can be calculated, as follows:

$$\alpha = \frac{f_b - f_c}{2f_b - f_c} \tag{Eqn. (7)}$$

$$\beta = \frac{f_c}{f_t} (\alpha - 1) - (1 + \alpha) \tag{Eqn. (8)}$$

where, f_b is the biaxial compressive strength, and f_t is the uniaxial tensile strength. The uniaxial compressive and tensile strength for different concrete grades considered in this paper are listed in Table 1. The ratio between f_b and f_c is assumed as 1.16.

The soil-pile interaction was modeled using discrete contact elements along the pile length and at the bottom of the pile. Similar approach was used in modeling of structural connectors [37,38]. This simplification for the soil model seems reasonable since the study mainly focuses on structural performance. Previous studies clearly indicate that the effect of the soil constraint is insignificant for the concrete pile with a large thickness [9]. The lateral pressure and friction from the soil were introduced through the contact element along the pile length. Negative gaps were used to model the initial geostatic state. A nonlinear softening contact model was used to mimic the soil's lateral response based on the API method following Eqn. (9) [35]:

$$p(y) = Ap_u \tanh\left(\frac{kzy}{Ap_u}\right) \tag{Eqn. (9)}$$

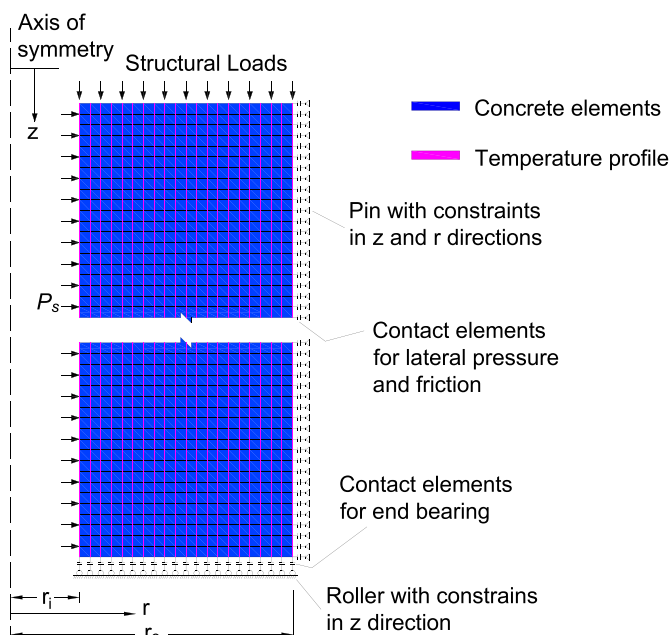


Fig. 5. 2D axisymmetric model for the mechanical analysis.

where, $p(y)$ is the lateral pressure from the soil; y is the soil lateral deformation; k is the initial modulus, taken as $24,400 \text{ kN/m}^3$ for the medium dense sand considered in this paper; A is a pile geometry factor taken as $0.3-0.8L_p/d_o$. z is the depth of the soil. p_u is the ultimate soil lateral resistance and can be calculated as:

$$p_u = \min\left(\frac{(C_1z + C_2d_o)\gamma'z}{C_3D\gamma'z}\right) \quad \text{Eqn. (10)}$$

where constant C_1 , C_2 , and C_3 are taken as 1.87, 2.62, and 29.65 for the medium dense sand considered in this paper. γ' is the density of the soil. The input soil response curves at selected depths for the lateral response of the contact element is shown in Fig. 6a.

The classical Coulomb friction model was adopted for the soil friction response following Eqn. (11) [36]:

$$\tau(z') = 0.1K\gamma'z\tan\delta \leq K\gamma'z\tan\delta \quad \text{Eqn. (11)}$$

where K is the coefficient of the lateral soil pressure, taken as 0.4; δ is the friction angle between the pile and soil interaction, taken as 25° . The input soil response curves at selected depths for the friction response of the contact element is shown in Fig. 6b.

The properties of the contact element at the bottom followed a simplified soil bearing response developed in Loehr and Brown [36]. The simplified soil bearing model for the medium dense sand considered in this paper follows a multi-linear lines with an ultimate bearing capacity of 1.64 MPa as shown in Fig. 6c.

4. Analytical results

4.1. Results from heat transfer analyses

This section presents the temperature profile inside the concrete pile section from the heat transfer analysis. Fig. 7 shows the temperature vs. loading cycle (n) at different locations of the concrete pile section for a case with $s = 5 \text{ m}$, $d_i = 200 \text{ mm}$, and $T_{s,max} = 39^\circ\text{C}$. As seen in Fig. 7a, the temperature history at the inner surface ($r = 0.1 \text{ m}$) follows the storage temperature shown in Fig. 3a. As the heat is transferred from the inner surface to the outer, the temperature in the pile section increases with the loading cycle (n) as shown in Fig. 7b. This cumulative temperature increase results in changes in the temperature distribution inside the concrete pile section. Fig. 8 shows the temperature distribution in different loading cycles at the middle of the cycle corresponding to the time at 19:00 as shown in Fig. 3, when the T_s reached the peak and those at the end of the cycle corresponding to the time at 7:00 (next day) as shown in Fig. 3 for the same case. The temperature distributions at two different times are completely different, and they change with the increase of the loading cycle (n). Such changes in the temperature

distribution cause different temperature gradients, which will, in turn, affect the stress state in the concrete pile section.

The pile spacing (s) and inner diameter (d_i) affect the temperature profile of the pile section. Fig. 9(a) and (b) show the maximum temperature in each loading cycle at the outer surface of the pile for different pile spacing (s) and different pile inner diameters (d_i), respectively. All the cases have a similar storage temperature ($T_{s,max}$). As seen in Fig. 9a, the temperature of the smaller pile spacing increases faster than that of the larger pile spacing due to the heat transferred from adjacent piles. As seen in Fig. 9b, the pile with a larger inner diameter has a faster temperature increase than the smaller case. This trend is because for a same pile outer diameter as studied in this paper, the larger inner diameter case has a thinner pile section which can transfer the heat faster than the smaller inner diameter case. These findings are consistent with the previous research [20,39].

4.2. General structural response from thermal-mechanical analyses

This section uses a case with $s = 5 \text{ m}$, $d_i = 200 \text{ mm}$, C150 concrete, and $T_{s,max} = 39^\circ\text{C}$ to demonstrate the general structural response of the pile section from the thermal-mechanical analysis. The pile was subjected to the combined structural, cyclic storage pressure, and cyclic thermal-mechanical loadings up to 70 cycles.

For the first 5 loading cycles in the pile section, Fig. 10 shows the time history of major stress components (σ_r , σ_v , and σ_θ) at the inner and outer surfaces. The stresses were plotted at locations where maximum stresses occur along the length of the pile. To investigate the effect of the thermal-mechanical loading, Fig. 10 indicates stresses from the storage pressure loading (P), the thermal-mechanical loading (T), and the combined loading (P + T).

As seen in Fig. 10(a) and (d), the storage pressure causes compression stresses in the radial direction which has a larger value in the inner surface than the outer surface. The thermal-mechanical loading increases the compression stress in this direction. The changes in the stress with the loading cycles are not significant. Since the concrete section is under a relatively small compression comparing to its strength, it will not cause safety issues in this direction.

As seen in Fig. 10(c) and (f), the storage pressure causes tensile stresses in the circumferential direction at both the inner and outer surfaces while the stress is larger at the inner surface. On the other hand, the thermal-mechanical loading generates compression stresses at the inner surface but tensile stresses at the outer surface as predicted in Sec. 2.2. The P + T combined loading produces smaller tensile stress than that induced from the storage pressure loading. As the loading cycle (n) increases, the circumferential stress at the inner surface gradually reduces in amplitude and changes to tension at the end/beginning of each loading cycle after several cycles. On the other hand, the amplitude of the tensile stress at the outer surface gradually reduces. This cumulative

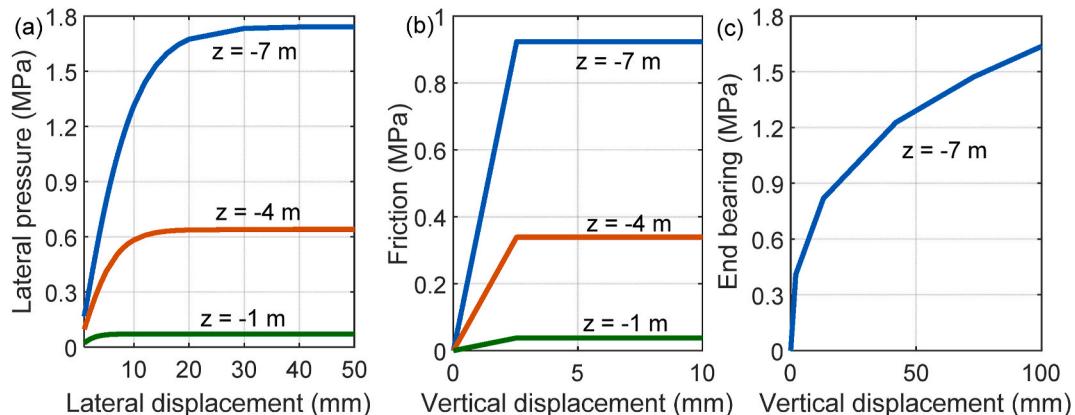


Fig. 6. Soil input response curves: (a) lateral pressure, (b) friction, and (d) end bearing.

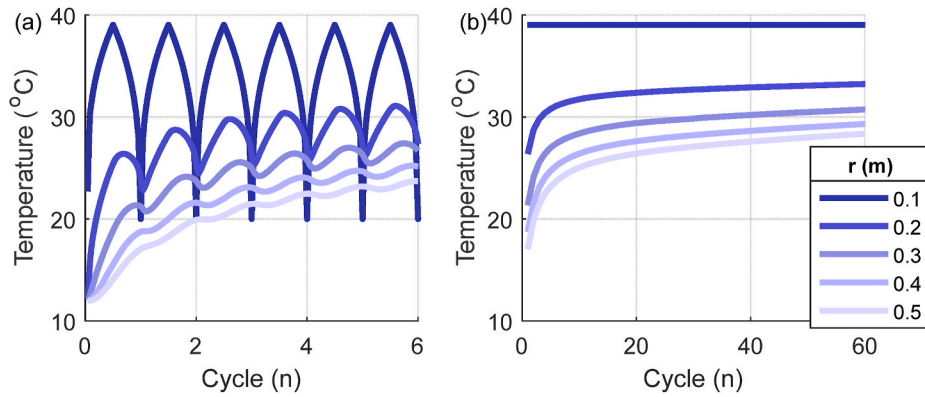


Fig. 7. Temperature at different locations of the concrete pile section: (a) time history; (b) maximum in each cycle.

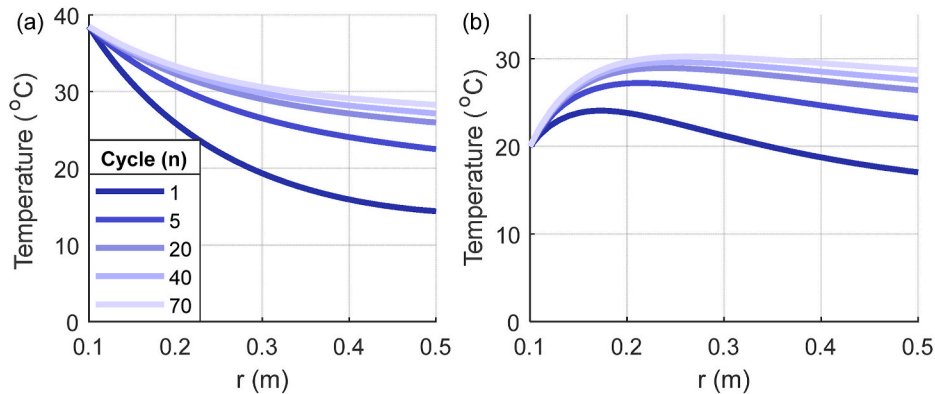


Fig. 8. Temperature distributions in different loading cycles: (a) at the middle of the cycle; (b) at the end of the cycle.

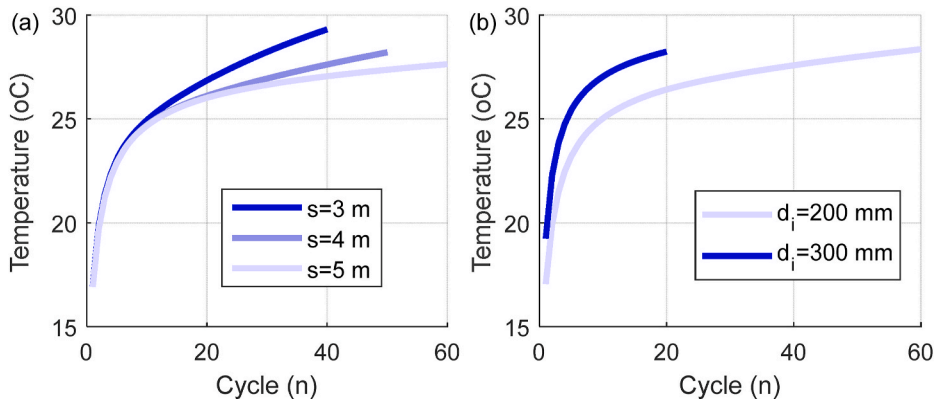


Fig. 9. Maximum temperature at the outer surface: (a) for different pile spacing (s); (b) for different pile inner diameters.

stress change with the loading cycle is because of the change in temperature gradient observed in the heat transfer analysis (refer to Fig. 8).

As seen in Fig. 10(b) and (e), the storage pressure loading along with the structural loading only generates negligible compression stresses in the vertical direction. However, the thermal-mechanical loading causes similar stress patterns in the vertical direction as in the circumferential direction, although the magnitude in the vertical direction is smaller. In summary, in the first several loading cycles, the combined loading (P + T) generates smaller tensile stresses than the storage pressure loading (P). A biaxial tensile stress state is observed in the combined loading while not occurring under the storage pressure loading. Since the concrete strength under biaxial tensile stresses is similar to that under uniaxial tensile stresses [29], the combined loading may still produce a

less critical stress state on the concrete than the storage pressure loading.

Fig. 11 shows stress distributions along the radial direction (r) under the combined loading at different times (beginning/end, middle, transition time) in different loading cycles for the circumferential (σ_θ , Fig. 11a, b, and 11c) and the vertical (σ_v , Fig. 11d, e, and 11f) stresses. The stress distribution under the storage pressure loading is indicated as green lines as a reference (the solid line is from finite element analysis and the dashed line is from Lamé's theory).

As seen in Fig. 11(a) and (b), the stress at the inner surface continuously increases (from compression to tension) while the stress at the outer surface reduces with the loading cycle. After sufficient loading cycles (i.e., $n = 70$ for this case), the tensile stress at the inner surface almost reaches the same value from the storage pressure loading (See

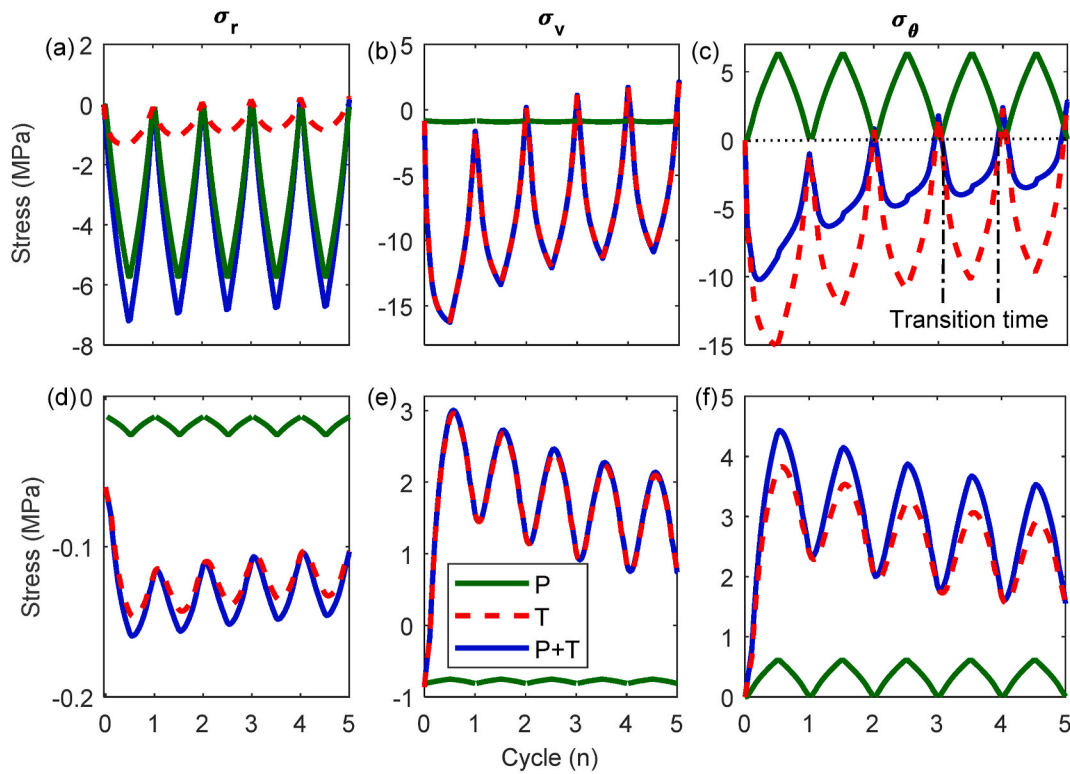


Fig. 10. Stress history in the pile section: (a) σ_r , (b) σ_v , (c) σ_θ at the inner surface; and (d) σ_r , (e) σ_v , (f) σ_θ at the outer surface.

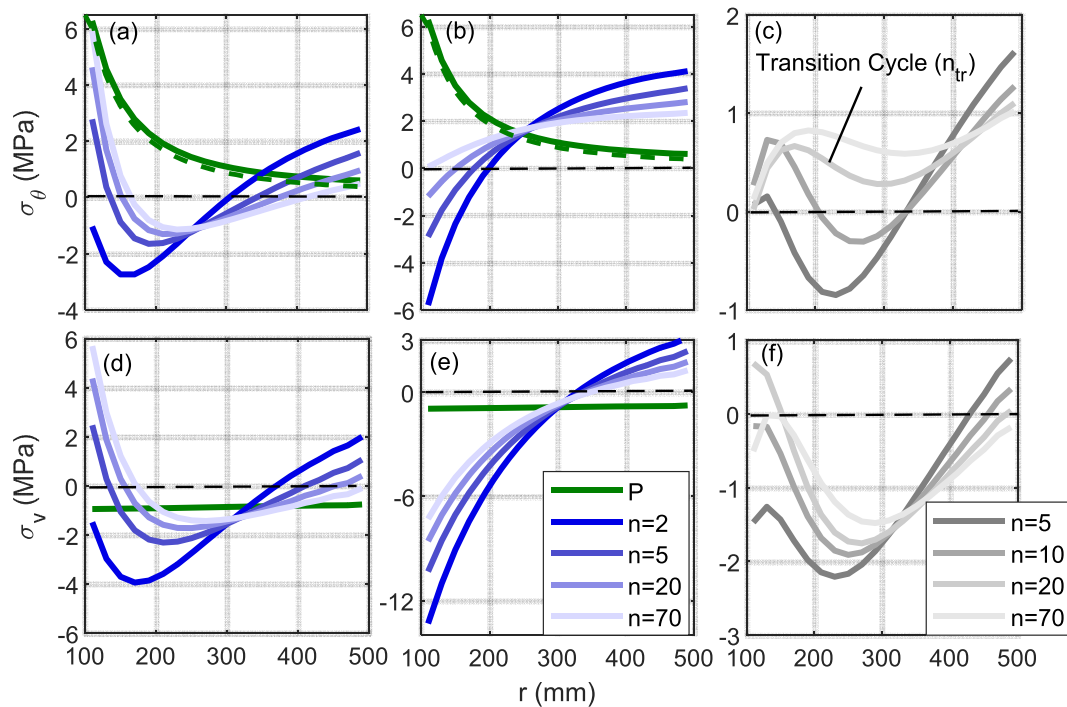


Fig. 11. Stress distributions along the radial direction in different loading cycles: (a) at the beginning of the cycle; (b) at the middle of the cycle; (c) near transition time for σ_θ , and (d) at the beginning of the cycle; (e) at the middle of the cycle; (f) near transition time for σ_v .

Fig. 11a). The stress distribution along the radial direction is a combined tension-compression distribution at the beginning and the middle of a cycle while the storage pressure produces a pure tensile stress distribution. After passing through sufficient loading cycles (i.e., $n = 70$ for this case), this combined tension-compression distribution changes to a pure tension when the stress at the inner surface becomes tension at the

middle of the cycle (See Fig. 11b).

After several loading cycles, the stress at the inner surface becomes tension at the beginning of the cycle while it remains compression at the middle of the cycle as shown in Fig. 11(a), (b), 11(d), and 11(e). Therefore, it confirms that there is a transition time when the stress at the inner surface changes from tension to compression within a certain

cycle, vice versa (Refer to Fig. 10c). Fig. 11c shows the circumferential stress distribution near this transition time. As the loading cycle increases, the stress distribution near the transition time changes from a combined tension-compression to a pure tension distribution. The loading cycle at this change is defined as a transition cycle (n_{tr}). If the loading cycle is less than the n_{tr} , the pure tensile stress distribution can be avoided. Similar trends can be observed in the vertical stress with smaller magnitudes in tension as shown in Fig. 11(d), (e) and 11(f). The pure tensile stress distribution does not occur near the transition time even after many loading cycles.

Fig. 12 show the response distribution along the vertical direction (z) for the vertical stress (σ_v), the circumferential stress (σ_θ), and the lateral expansion displacement. As seen in Fig. 12a and b, the stress distribution along the vertical direction (z) is reasonably uniform except that lower stresses are observed near the top and bottom of the pile. Fig. 12c indicates that the lateral expansion displacement is not significant which proves the small displacement assumption made in the model.

Fig. 13 show the soil response profile along the vertical direction at the end of different loading cycles for (a) lateral pressure, (b) friction, and (c) vertical displacement. As a reference, the soil response profile under the structural loading is indicated as black dashed lines. The lateral pressure increases with the loading cycle. The friction stress reduces at the top portion of the pile and increases at the bottom portion of the pile due to the elongation of the pile under thermal-mechanical loading. This elongation reduces the vertical displacement at top part of the pile as indicated in Fig. 13(c). However, the changes in the soil response are not significant due to a relatively large concrete section.

4.3. Structural response under different magnitudes of the storage temperature

As discussed in the previous section, the thermal-mechanical loading has the potential to reduce the critical tensile stress and avoid unfavorable pure tensile stress distribution inside the concrete pile section. However, limiting the loading cycle (n) is important since the tensile stress can gradually increase, and the stress distribution can be changed after a certain amount of the loading cycle. Therefore, this section discusses the determination of an optimal storage temperature ($T_{s,opt}$) and an allowable loading cycle (n_{all}) by examining the pile section's maximum stresses under different storage temperatures for a case with $s = 5$ m, $d_i = 200$ mm, and C150 concrete.

Fig. 14 shows the maximum stresses vs. the loading cycle (n) under different magnitudes of the storage temperature ($\gamma = 1.5\%$, 1.75% , and 2.25% , refer to Fig. 3a) in terms of the vertical stress (σ_v), the circumferential stress (σ_θ), and the yield function $F(\sigma)$, respectively. As a reference, the maximum stress under the storage pressure loading is indicated as a solid green line. The tensile or compression strength of the concrete with a safety factor (SF) of 1.5 is indicated as black dotted lines. The stress at the inner surface is shown as solid lines while the stress at

the outer surface is indicated as dashed lines.

As seen in Fig. 14(a) and (b), the maximum stresses increase at the inner surface but reduces at the outer surface with the loading cycle. These stresses at the inner surface eventually exceed the strength of the concrete after a certain amount of loading cycles. As the storage temperature increases, the loading cycle, where the stress exceeds the strength, decreases. Particularly, the stress at the outer surface can reach the strength limit at the 1st cycle when the storage temperature is high enough (See. $\gamma = 2.25\%$ in Fig. 14b).

Comparing to the storage pressure loading, the combined loading case can limit the maximum stress to be less than the concrete strength if a proper storage temperature and a loading cycle are applied. However, the combined loading case also produces a biaxial tensile stress state while the storage pressure loading generates only uniaxial tensile stress. Therefore, it is essential to investigate the yield function $[F(\sigma)]$ under the multi-axial stress state. Figure 14(c) shows the maximum $F(\sigma)$ vs. the loading cycle. A loading cycle limit, termed as n_{lim} , can be identified as the intersection between the $F(\sigma)$ and f_c/SF for a given storage temperature as illustrated in Fig. 14(c). On the other hand, a Matlab code was developed to identify the transition cycle (n_{tr} , refer to Fig. 11c) for a given storage temperature when the stress distribution changes to pure tension. Fig. 15 plots the loading cycle limit and the transition cycle vs. $T_{s,max}$. As presented in Fig. 15, the loading cycle limit decreases as the storage temperature increases, which is consistent with the trend shown in Fig. 14. The transition cycle slightly increases with the increase of the storage temperature. Therefore, it is possible to identify an intersection between the two curves as illustrated in Fig. 15. The coordinates of this intersection are defined as the optimal storage temperature ($T_{s,opt}$) and the allowable loading cycle (n_{all}). This intersection implies that the energy storage pile foundation ($s = 5$ m, $d_i = 200$ mm, and C150 concrete) designed with the $T_{s,opt}$ can safely operate n_{all} cycles: the maximum stress in the concrete section during the operation will be safely under its strength limit, and the concrete section will not undergo a pure tension stress distribution.

After continuously operating for n_{all} cycles, the energy storage operation needs to be paused for one day to have the temperature and the stress in the pile foundation recovering to their initial conditions. Fig. 16 shows the circumferential stress history for the pile subjected to two allowable loading cycles with a one-day pause. As seen in Fig. 16, the stresses can restore to their initial conditions within one day and repeat the same history during the second allowable cyclic loading.

4.4. Parametric results

This section summarizes the effects of the studied parameters on the structural response of the energy storage pile foundation under the combined structural, storage pressure, and thermal-mechanical loadings.

Fig. 17 shows the maximum tensile stresses vs. the loading cycle for

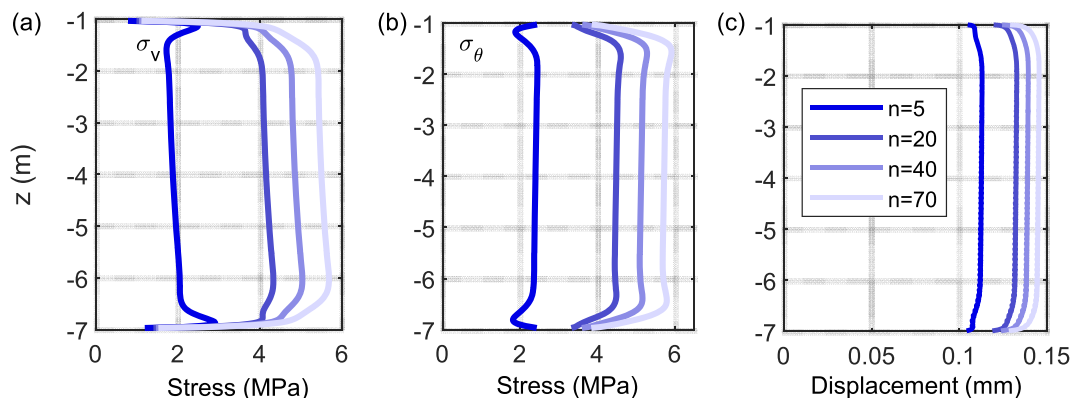


Fig. 12. Vertical response distributions in different loading cycles: (a) σ_v ; (b) σ_θ ; (c) lateral expansion.

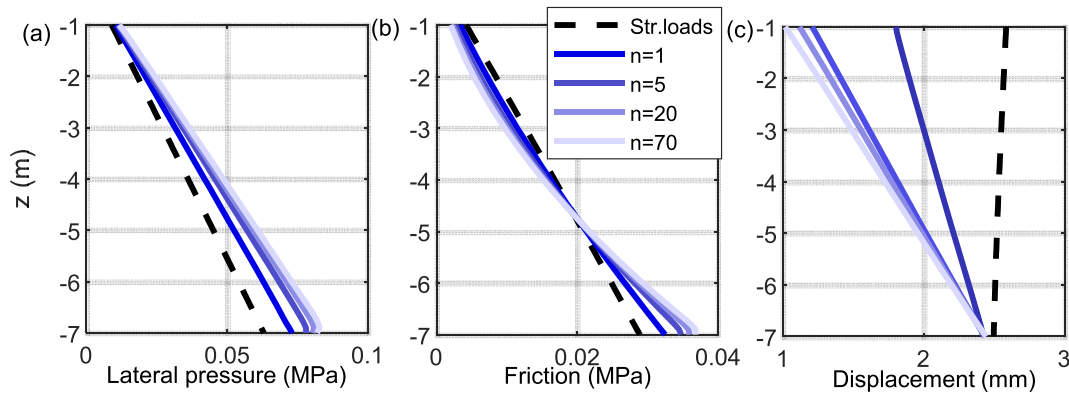


Fig. 13. Soil response distributions along the vertical direction in different loading cycles: (a) lateral pressure; (b) friction; (c) vertical displacement.

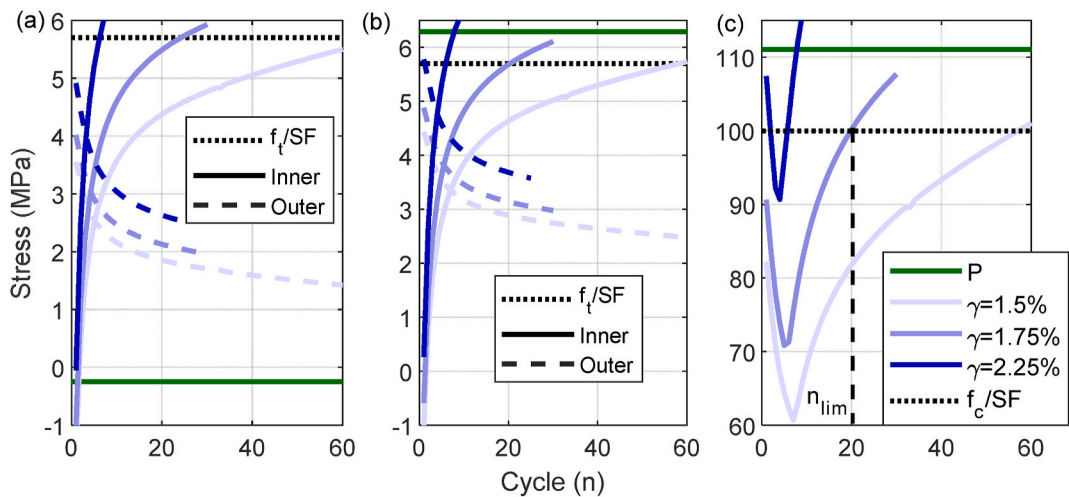


Fig. 14. Maximum stresses vs. the loading cycle (n) under different magnitudes of the storage temperature: (a) σ_v ; (b) σ_{θ} , and (c) $F(\sigma)$.

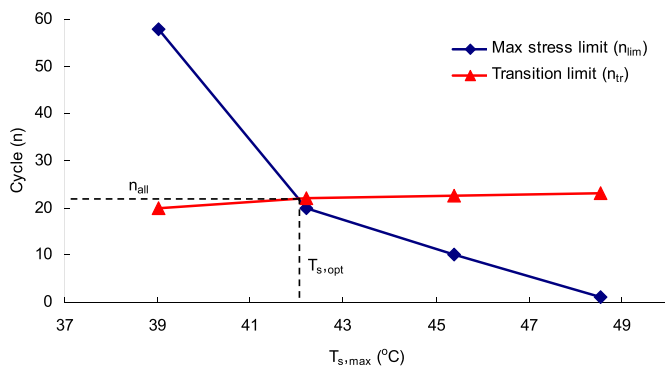


Fig. 15. Determination of the optimal storage temperature and the allowable loading cycle.

different concrete grades at a similar storage temperature ($T_{s,max} \approx 39^\circ\text{C}$) for a case with $s = 5\text{ m}$ and $d_i = 200\text{ mm}$. Since the concrete pile was modeled as elastic elements, the actual difference in the model is the Young's modulus for different concrete grades as listed in Table 1. As seen in Fig. 17, the concrete pile with a lower grade and Young's modulus shows lower maximum tensile stresses than the one with a higher grade and Young's modulus. This trend is because the lower Young's modulus generates smaller thermal stresses. However, the strength of the concrete is also different for different concrete grades as indicated in Fig. 17. Therefore, the n_{lim} is not necessarily larger for the

lower grade concrete at a given storage temperature. As seen in Fig. 17 (c), the lower concrete grade cases (C60 and C100) reach the strength limit at the outer surface at the 1st cycle.

Fig. 18 shows the maximum tensile stresses vs. the loading cycle for different pile spacing (s) at a similar storage temperature ($T_{s,max} \approx 41^\circ\text{C}$) for a case with C150 concrete and $d_i = 200\text{ mm}$. As seen in Fig. 18, the maximum stress is similar for different pile spacing at the beginning of the loading. As the loading cycle increases, the pile with a smaller spacing shows larger stress than the pile with a large spacing, which is consistent with the maximum temperature values observed in the heat transfer analysis (Refer to Fig. 9a). This trend indicates that the pile with a smaller spacing has a smaller n_{lim} than the pile with a larger spacing for a given storage temperature.

Fig. 19 shows the maximum tensile stresses vs. the loading cycle for piles with different inner diameters (d_i) at a similar storage temperature ($T_{s,max} \approx 39^\circ\text{C}$) for a case with C150 concrete and $s = 5\text{ m}$. As seen in Fig. 19, the pile with a larger d_i shows larger stress than the pile with a smaller d_i , which is consistent with the maximum temperature values observed in the heat transfer analysis (Refer to Fig. 9b). This trend indicates that the pile with a larger d_i has a smaller n_{lim} than the pile with a smaller d_i for a given storage temperature.

5. Design recommendations

Following the same procedure used in Sec. 4.3, the optimal storage temperature ($T_{s,opt}$) and the allowable loading cycle (n_{all}) can be determined for all the cases considered in this paper. With these calculated $T_{s,opt}$ and n_{all} , a design chart for the energy storage pile foundation

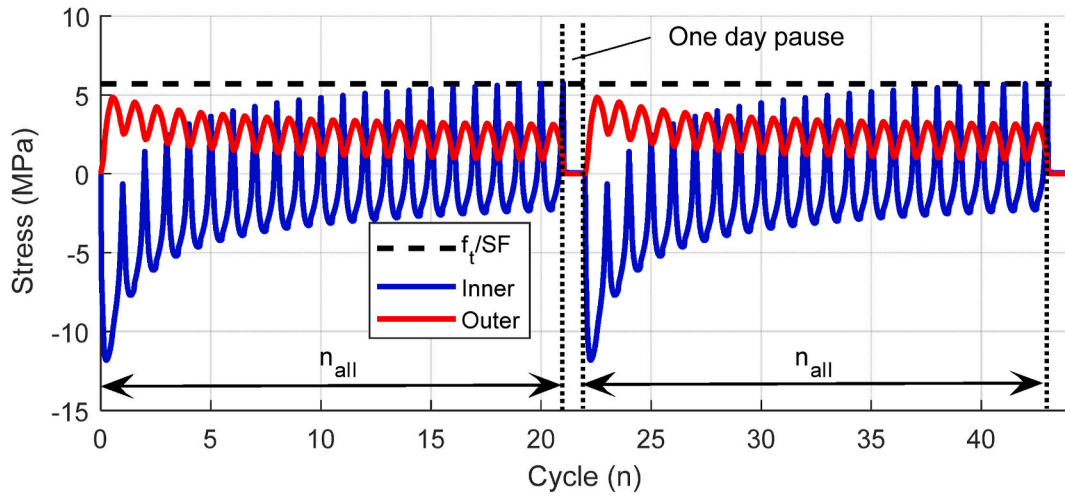


Fig. 16. Circumferential stress history with one-day pauses operation.

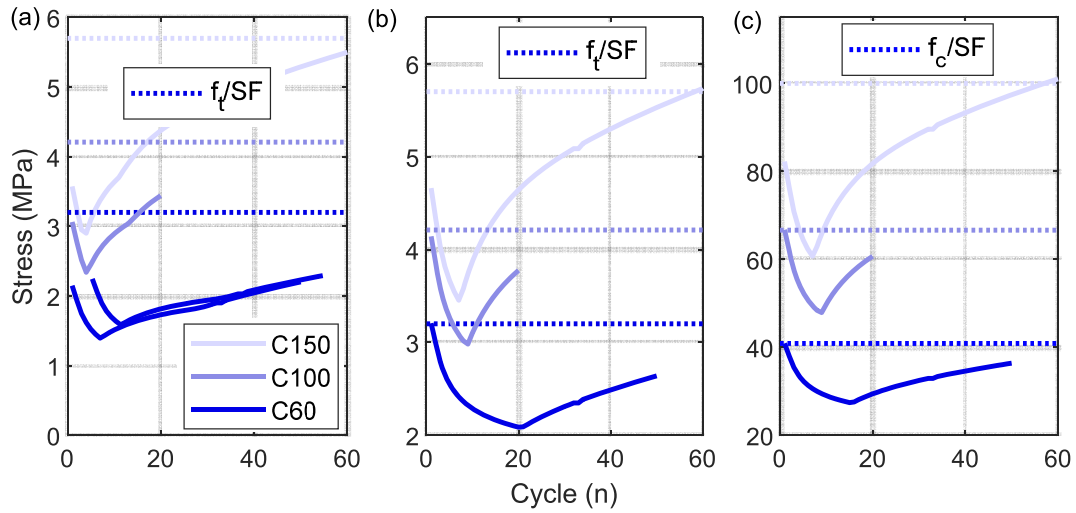


Fig. 17. Maximum tensile stresses vs. the loading cycle (n) for different concrete grades: σ_v ; (b) σ_θ , and (c) $F(\sigma)$.

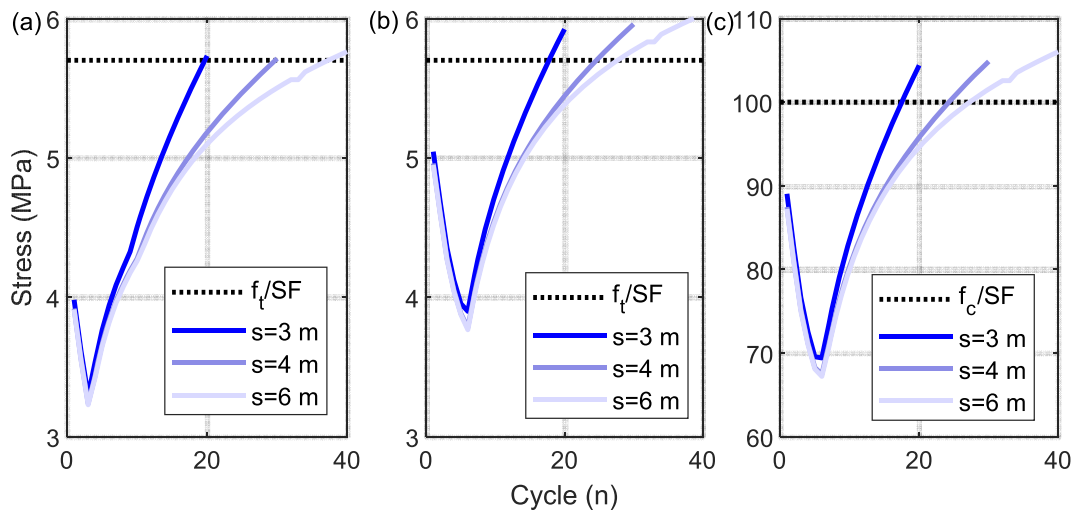


Fig. 18. Maximum tensile stresses vs. the loading cycle (n) for different pile spacing: σ_v ; (b) σ_θ , and (c) $F(\sigma)$.

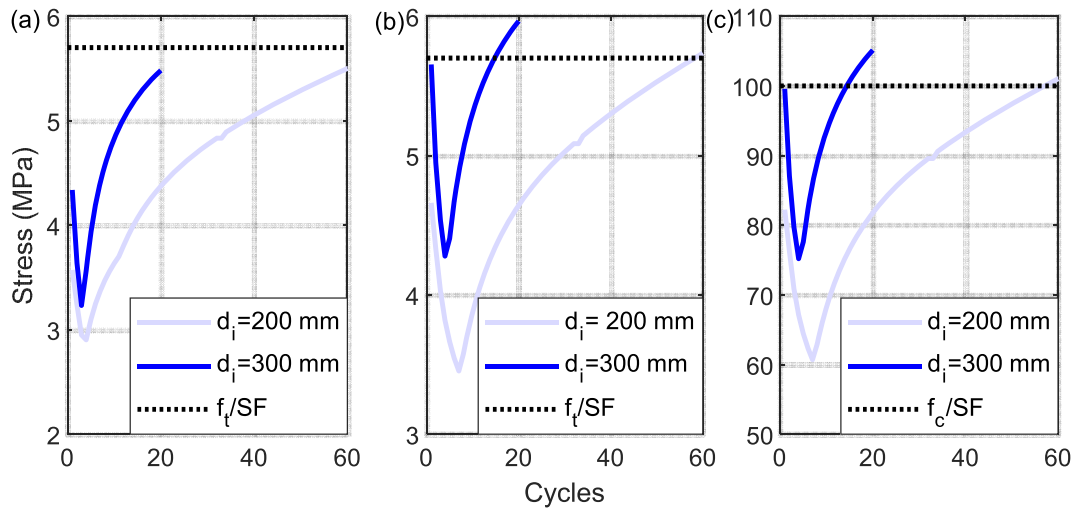


Fig. 19. Maximum tensile stresses vs. the loading cycle (n) for different d_i : (a) σ_v ; (b) σ_θ , and (c) $F(\sigma)$.

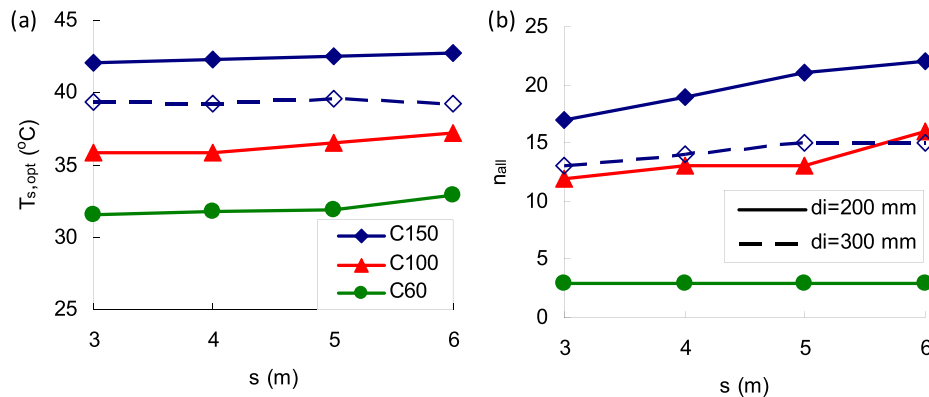


Fig. 20. Design charts for the energy storage pile foundation: (a) $T_{s,opt}$, (b) n_{all} .

can be developed, as shown in Fig. 20.

As seen in Fig. 20a, the optimal storage temperature slightly increases with the increase of the pile spacing. The pile with a higher concrete grade and a smaller inner diameter has a higher optimal storage temperature. As seen in Fig. 20(b), the allowable loading cycle typically increases with the increase of the pile spacing. The pile with a higher concrete grade and a smaller inner diameter has a larger allowable loading cycle. These trends are consistent with the results presented in Sec. 4.4. In order to have a longer, uninterrupted operation, it is recommended to use higher concrete strength (C100 or C150) and a smaller pile inner diameter ($d_i = 200$ mm) for the energy storage pile foundations.

6. Conclusions

This paper explores the feasibility of the energy storage pile foundation with a storage temperature higher than the ambient temperature through analytical studies. The analytical study was conducted under cyclic loadings through an uncoupled sequential nonlinear dynamic heat transfer and static thermal-mechanical analyses. The structural responses of the energy storage pile foundation subjected to the combined structural, storage pressure, and thermal-mechanical loadings were investigated from the analysis results. The following conclusions can be made from the heat transfer analysis:

- (1) The increase in the storage temperature results in temperature gradients in the pile section. The temperature gradient changes with the loading cycles due to the cumulative heat transfer effect.
- (2) The smaller pile spacing and larger pile inner diameter can result in a faster heat transfer and a larger temperature change in the pile section with the increase of the loading cycle.

The following conclusions can be made from the thermal-mechanical analysis:

- (1) The thermal-mechanical loading produces a different stress distribution comparing to the storage pressure loading. The combined loading results in a lower maximum tensile stress and a more favorable compression-tension stress distribution in the pile section than the storage pressure loading within a certain amount of loading cycles.
- (2) The tensile stress under the combined loading increases with the increase of the loading cycle due to the temperature gradient changes. After sufficient loading cycles, the tensile stress under the combined loading may exceed the value under the storage pressure loading.
- (3) The stresses in the pile section under the combined loading may change to a pure tension distribution at the transition time after sufficient loading cycles.
- (4) The thermal-mechanical loading produces a biaxial tensile stress state while the storage pressure loading generates only a uniaxial tensile stress state. Although the concrete has similar strength

under uniaxial and biaxial tensile loadings, it is important to check the yield surface under a multi-axial stress state.

- (5) An optimal storage temperature and an allowable loading cycle can be identified for the energy storage pile foundation, which implies that the pile designed with this optimal temperature can safely operate for this allowable loading cycle. Afterward, the energy storage operation needs to be paused for one day to have the temperature and the stress in the pile section recovering to their initial conditions.
- (6) The higher Young's modulus, smaller pile spacing, and larger pile inner diameter can generate higher tensile stresses inside the pile section as the increase of loading cycle.

The analysis results developed design charts for the energy storage pile foundation to determine the optimal storage temperature and the allowable loading cycle for different pile design parameters considered in this paper. In order to have a longer uninterrupted operation, it is recommended to use higher concrete strength (C100 or C150) and a smaller pile inner diameter ($d_i = 200$ mm) for the energy storage pile foundations.

Authors' contributions

Conceptualization (DZ, JK); Data curation (MB); Formal analysis (MB); Funding acquisition (DZ, DL); Investigation (DZ, MB); Methodology (DZ, CS); Project administration (DZ, JK, DL); Supervision (DZ, JK); Validation (MB); Visualization (DZ, MB); Roles/Writing - original draft (MB, DZ); Writing - review & editing (DZ, JK, CS, DL)

Declaration of competing interest

The authors declare that they have no known competing financial interests or personal relationships that could have appeared to influence the work reported in this paper.

Acknowledgements

Nazarbayev University funded this research under Faculty Development Competitive Research Grant No. 021220FD2151. The authors are grateful for this support. Any opinions, findings, conclusions, or recommendations expressed in this material are those of the author(s) and do not necessarily reflect the views of Nazarbayev University. The authors would also like to thank you for the support from the National Research Foundation of Korea (NRF) grant funded by the Korean government (MSIT) (No. 2020R1F1A1048422).

References

- [1] A.K. Sani, R.M. Singh, T. Amis, I. Cavarretta, A review on the performance of geothermal energy pile foundation, its design process and applications, *Renew. Sustain. Energy Rev.* 106 (2019) 54–78.
- [2] L. Laloui, M. Nuth, L. Vulliet, Experimental and numerical investigations of the behaviour of a heat exchanger pile, *Int. J. Numer. Anal. Methods Geomech.* 30 (8) (2006) 763–781.
- [3] K.D. Murphy, J.S. McCartney, K.S. Henry, Evaluation of thermo-mechanical and thermal behavior of full-scale energy foundations, *Acta Geotechnica* 10 (2) (2015) 179–195.
- [4] A. Di Donna, A.F.R. Loria, L. Laloui, Numerical study of the response of a group of energy piles under different combinations of thermo-mechanical loads, *Comput. Geotech.* 72 (2016) 126–142.
- [5] M. Faizal, A. Bouazza, J.S. McCartney, C. Haberfield, Effects of cyclic temperature variations on thermal response of an energy pile under a residential building, *J. Geotech. Geoenviron. Eng.* 145 (10) (2019), 04019066.
- [6] L. Zhang, S. Ahmari, B. Sternberg, M. Budhu, Feasibility study of compressed air energy storage using steel pipe piles, in: *GeoCongress 2012: State of the Art and Practice in Geotechnical Engineering*, 2012, pp. 4272–4279.
- [7] J. Rugolo, M.J. Aziz, Electricity storage for intermittent renewable sources, *Energy Environ. Sci.* 5 (5) (2012) 7151–7160.
- [8] D. Wu, J.G. Wang, B. Hu, S.Q. Yang, A coupled thermo-hydro-mechanical model for evaluating air leakage from an unlined compressed air energy storage cavern, *Renew. Energy* 146 (2020) 907–920.
- [9] D. Zhang, J. Kim, S. Tulebekova, D. Saliyev, D. Lee, Structural responses of reinforced concrete pile foundations subjected to pressures from compressed air for renewable energy storage, *Int. J. Concrete Struct. Mater.* 12 (1) (2018) 1–16.
- [10] S. Tulebekova, D. Zhang, D. Lee, J.R. Kim, T. Barissov, V. Tsoy, Nonlinear responses of energy storage pile foundations with fiber reinforced concrete, *Struct. Eng. Mech.* 71 (4) (2019) 363–375.
- [11] J. Ko, S. Kim, S. Kim, H. Seo, Utilizing building foundations as micro-scale compressed air energy storage vessel: numerical study for mechanical feasibility, *J. Energy Storage* 28 (2020), 101225.
- [12] J. Zhang, H. Seo, S. Kim, J. Ko, S. Kim, Experimental study of pipe-pile-based micro-scale compressed air energy storage (PPMS-CAES) for a building, in: *E3S Web of Conferences*, vol. 205, EDP Sciences, 2020, p. 7012.
- [13] A. Agibayeva, D. Lee, H. Ju, D. Zhang, J.R. Kim, Application of steel-concrete composite pile foundation system as energy storage medium, *Struct. Eng. Mech.* 77 (6) (2021) 753–763.
- [14] D. Wolf, M. Budt, LTA-CAES—a low-temperature approach to adiabatic compressed air energy storage, *Appl. Energy* 125 (2014) 158–164.
- [15] Y.M. Kim, J.H. Lee, S.J. Kim, D. Favrat, Potential and evolution of compressed air energy storage: energy and exergy analyses, *Entropy* 14 (8) (2012) 1501–1521.
- [16] E.J. Hearn, *Mechanics of Materials 1: The Mechanics of Elastic and Plastic Deformation of Solids and Structural Materials*, Elsevier, 1997.
- [17] C. Evcı, M. Gülgeç, Functionally graded hollow cylinder under pressure and thermal loading: effect of material parameters on stress and temperature distributions, *Int. J. Eng. Sci.* 123 (2018) 92–108.
- [18] A.R. Shahani, S.M. Nabavi, Analytical solution of the quasi-static thermoelasticity problem in a pressurized thick-walled cylinder subjected to transient thermal loading, *Appl. Math. Model.* 31 (9) (2007) 1807–1818.
- [19] A. Aziz, M. Torabi, Thermal stresses in a hollow cylinder with convective boundary conditions on the inside and outside surfaces, *J. Therm. Stresses* 36 (10) (2013) 1096–1111.
- [20] D. Sailauova, Z. Mamesh, D. Zhang, D. Lee, C.S. Shon, J.R. Kim, Group pile effect on temperature distributions inside energy storage pile foundations, *Appl. Sci.* 10 (18) (2020) 6597.
- [21] A.K.H. Kwan, S.H. Chu, Direct tension behaviour of steel fibre reinforced concrete measured by a new test method, *Eng. Struct.* 176 (2018) 324–336.
- [22] A.M.T. Hassan, S.W. Jones, G.H. Mahmud, Experimental test methods to determine the uniaxial tensile and compressive behaviour of ultra high performance fibre reinforced concrete (UHPC), *Construct. Build. Mater.* 37 (2012) 874–882.
- [23] M. Musmar, Tensile strength of steel fiber reinforced concrete, *Contemp. Eng. Sci.* 6 (5) (2013) 225–237.
- [24] T. Al Shemmeri, *Engineering Thermodynamics*, Tarik Al-Shemmeri & Ventus Publishing ApS, 2010.
- [25] J.M. Campbell, L. Lilly, R. Maddox, *Gas conditioning and processing*, 2, in: *PennWell Conferences and Exhibitions*, vol. 3, 1999, November. Houston, TX (United States).
- [26] R.M. Assunção, *Thermal and Thermal-Mechanical Analysis of Thermo-Active Pile Foundations*, IST, University of Lisbon, 2014.
- [27] H. Brandl, Energy foundations and other thermo-active ground structures, *Geotechnique* 56 (2) (2006) 81–122.
- [28] V. Kodur, W. Khaliq, Effect of temperature on thermal properties of different types of high-strength concrete, *J. Mater. Civ. Eng.* 23 (6) (2011) 793–801.
- [29] W. Zheng, B. Luo, Y. Wang, Microstructure and mechanical properties of RPC containing PP fibres at elevated temperatures, *Mag. Concr. Res.* 66 (8) (2014) 397–408.
- [30] N.H. Abu-Hamdeh, Thermal properties of soils as affected by density and water content, *Biosyst. Eng.* 86 (1) (2003) 97–102.
- [31] S.K. Haigh, Thermal conductivity of sands, *Geotechnique* 62 (7) (2012) 617–625.
- [32] H.R. Thomas, S.W. Rees, Measured and simulated heat transfer to foundation soils, *Geotechnique* 59 (4) (2009) 365–375.
- [33] B.A. Graybeal, Material property characterization of ultra-high performance concrete (No. FHWA-HRT-06-103). United States, in: *Federal Highway Administration, Office of Infrastructure Research and Development*, 2006.
- [34] J. Lee, G.L. Fenves, Plastic-damage model for cyclic loading of concrete structures, *J. Eng. Mech.* 124 (8) (1998) 892–900.
- [35] K.T. Brødbæk, M. Møller, S.P.H. Sørensen, A.H. Augustesen, *Review of Py Relationships in Cohesionless Soil*, 2009.
- [36] E. Loehr, D. Brown, A Method for Predicting Mobilization Resistance for Micropiles Used in Slope Stabilization Applications. A Report Prepared for the Joint ADSC/DFI Micropile Committee, 2008.
- [37] G. Wan, R.B. Fleischman, D. Zhang, Effect of spandrel beam to double tee connection characteristic on flexure-controlled precast diaphragms, *Journal of Structural Engineering* 138 (2) (2012) 247–257, [https://doi.org/10.1061/\(ASCE\)ST.1943-541X.0000426](https://doi.org/10.1061/(ASCE)ST.1943-541X.0000426).
- [38] D. Zhang, R.B. Fleischman, Establishment of performance-based seismic design factors for precast concrete floor diaphragms, *Earthquake Engineering and Structural Dynamics* 45 (5) (2016) 675–698, <https://doi.org/10.1002/eqe.2679>.
- [39] D. Zhang, Z. Mamesh, D. Sailauova, C.-S. Shon, D. Lee, J.R. Kim, Temperature distributions inside concrete sections of renewable energy storage pile foundations, *Applied Sciences* 9 (22) (2019), <https://doi.org/10.3390/app9224776>.

Notations

- A: = pile geometry factor
 C: = adiabatic constant
 d_i, d_o : = pile inner, outer diameter

E_c : = concrete Young's modulus
 $F(\sigma)$: = concrete yield function under multi-axial stresses
 f_b : = concrete biaxial compression strength
 f_t, f_c : = concrete tensile, compression strength
 I_1, J_2 : = first invariant, second deviatoric stress invariants
 K : = coefficient of the lateral soil pressure
 k : = soil initial modulus
 n : = loading cycle
 n_m, n_{all} : = transition, allowable loading cycle
 $p(y)$: = soil lateral pressure
 p_{ul} : = ultimate soil lateral resistance
 R : = universal gas constant
 s : = pile spacing
 T_1, P_1 : = ambient temperature, air pressure
 T_2, P_2 : = temperature, air pressure after the compression process
 T_3, P_3 : = storage temperature, pressure after the heating process
 T_s, P_s : = storage temperature, pressure
 T_{smax}, P_{smax} : = storage temperature, pressure at the peak during a 24-h cycle

$T_{s\ opt}$: = optimal storage temperature
 t_m : = compression time;
 u_z : = soil vertical displacement
 V_s : = available volume for storage
 w_m : = available energy for storage
 y : = soil lateral displacement
 z : = coordinate along the length of the pile measured from the ground
 α, β : = dimensionless constant for the concrete yield function
 δ : = friction angle between the pile and soil interaction
 γ : = cooling index
 γ' : = density of the soil
 η_1 : = compression efficiency
 μ : = molar mass of the air
 ρ_a : = ambient air density
 $\sigma_r, \sigma_y, \sigma_\theta$: = radial, vertical, circumferential stress
 $\hat{\sigma}_{max}$: = algebraically maximum principal stress